

Black Phosphorus and Two-Dimensional Hyperbolic Materials: Tunable Surface Plasmons, Green Function and Complex-Plane Analysis

S. Ali Hassani Gangaraj, Tony Low, Andrei Nemilentsau, George W. Hanson, *Fellow, IEEE*

Abstract—We study the electromagnetic response of two- and quasi-two-dimensional hyperbolic materials, on which a simple dipole source can excite a well-confined and tunable surface plasmon polariton (SPP). The analysis is based on the Green function for an anisotropic two-dimensional surface, which nominally requires the evaluation of a two-dimensional Sommerfeld integral. We show that for the SPP contribution this integral can be evaluated efficiently in a mixed continuous-discrete form as a continuous spectrum contribution (branch cut integral) of a residue term, in distinction to the isotropic case, where the SPP is simply given as a discrete residue term. The regime of strong SPP excitation is discussed, and complex-plane singularities are identified, leading to physical insight into the excited SPP. Examples are presented using graphene strips to form a hyperbolic metasurface, and thin-film black phosphorus (BP). The green function and complex-plane analysis developed allows for the exploration of hyperbolic plasmons in general 2D materials.

Index Terms—Hyperbolic surface, Anisotropy, Directed surface plasmon, Green function, Complex plane analysis.

I. INTRODUCTION

Recently, the development of nano-fabrication technologies has made it possible to fabricate artificial materials exhibiting a hyperbolic regime - hyperbolic metamaterials (HMTMs) [1], [2]. Hyperbolic metamaterials are uniaxial structures with extreme anisotropy, whose reactive effective material tensor components have opposite signs for orthogonal electric field polarizations [3]. Hyperbolic materials exhibit hyperbolic, as opposed to the usual elliptic, dispersion, and combine the properties of transparent dielectrics and reflective metals [1]. These exotic properties have led to new physical phenomena and to the proposal for optical devices for a wide range of applications, such as far-field subwavelength imaging, nanolithography, emission engineering [1], negative index waveguides [4], subdiffraction photonic funnels [5], and nanoscale resonators [6].

Manuscript received xxx; revised xxx.

Corresponding author: S. Ali Hassani Gangaraj is with Department of Electrical Engineering, University of Wisconsin-Milwaukee, Milwaukee, Wisconsin 53211, USA. (email: ali.gangaraj@gmail.com).

Tony Low is with Department of Electrical and Computer Engineering, University of Minnesota, Minneapolis, Minnesota 55455, USA. (email: tlow@umn.edu).

Andrei Nemilentsau is with Department of Electrical Engineering, University of Wisconsin-Milwaukee, Milwaukee, Wisconsin 53211, USA (email: andrei.nemilentsau@gmail.com).

George W. Hanson is with Department of Electrical Engineering, University of Wisconsin-Milwaukee, Milwaukee, Wisconsin 53211, USA. (email: george@uwm.edu).

The complexity of bulk fabrication of these materials has hindered the impact of this technology, especially for optical metamaterials, and volumetric effects may be detrimental for the associated losses [3]. Metasurfaces [7]-[8], sheets of material with extreme sub-wavelength thickness, might address many of the present challenges and allow integration with planarized systems compatible with integrated circuits. Many high frequency electronics applications are envisioned for metasurfaces due to their ability to support and guide highly confined surface plasmons. The class of two dimensional (2D) atomic crystals [9] represents the ultimate embodiment of a meta-surface in terms of thinness, and often performance (e.g. tunability, flexibility, quality factor). Some notable examples of 2D layered crystals include graphene, transition metal dichalcogenides, trichalcogenides, black phosphorus, boron nitride, and many more.

Graphene in particular has received considerable attention as a promising two-dimensional surface for many applications relating to large enhancement in Purcell emission, integrability, electronic tunability and transformation optics [10]-[17]. In addition to graphene, black phosphorus (BP) is also a layered material, with each layer forming a puckered surface due to sp³ hybridization. It is one of the thermodynamically more stable phases of phosphorus, at ambient temperature and pressure [18]. BP has recently been exfoliated into its multilayers [19]-[22], showing good electrical transport properties. In particular, the optical absorption spectra of BP vary sensitively with thickness, doping, and light polarization, especially across the technologically relevant mid- to near-infrared spectrum [23]-[25]. Hence, it has also received considerable attention for optoelectronics, such as hyperspectral imaging and detection [26]-[29], photodetectors in silicon photonics [30], photoluminescence due to excitonic effects [31], among many others.

Both natural materials and metasurfaces can be isotropic or anisotropic, and, e.g., isotropic graphene can be employed to form an effective anisotropic metasurface by modulating its conductivity [14], [3]. And, both natural materials and metasurfaces may exhibit a hyperbolic regime. In this work we analyze the surface plasmon on an anisotropic two-dimensional surface by evaluating the Sommerfeld integral based on the Green function for the structure. The nominally two-dimensional Sommerfeld integral form of the Green function is very time-consuming to evaluate, and provides no physical insight into the resulting field. Here we show that for the SPP field, this integral can be evaluated efficiently in

a mixed continuous-discrete form as a continuous spectrum contribution (branch cut integral) of a residue term. Complex-plane singularities are identified with various branch cut integrals, leading to physical insight into the excited SPP. For some two-dimensional materials the surface conductivity is rather weak, and a discussion is provided concerning the strength of the reactive conductivity response to maintain an SPP.

The paper is organized as follows. We discuss the Green function calculation for an anisotropic two-dimensional sheet with conductivity tensor $\underline{\sigma}$ in vacuum. A Hertzian dipole vertical current source serves as the excitation. Rigorous complex plane analysis is shown to reduce the two-dimensional iterated Sommerfeld integral to a residue for the inner integral, and a branch cut for the outer integral [32]-[35]. The relevant singularities are detailed. We show that graphene strips support propagation of directed surface waves and that the direction of propagation can be controlled by changing the frequency or doping. We also consider black phosphorus, which is dynamically tunable and anisotropic, and can be hyperbolic.

II. GREEN FUNCTION THEORY

The geometry under consideration is shown in Fig. 1. We consider an anisotropic layer with conductivity tensor

$$\underline{\sigma} = \begin{pmatrix} \sigma_{xx} & 0 \\ 0 & \sigma_{zz} \end{pmatrix} \quad (1)$$

embedded at the interface of two isotropic different materials with electrical properties ϵ_1, μ_1 and ϵ_2, μ_2 .

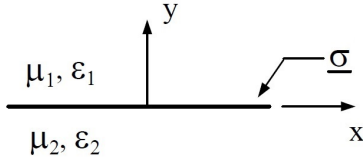


Fig. 1. Anisotropic surface with conductivity tensor $\bar{\sigma}$ at the interface of two isotropic materials.

For any planarly layered, piecewise-constant medium, the electric and magnetic fields in region n due to an electric current are

$$\mathbf{E}^{(n)}(\mathbf{r}) = (k_n^2 + \nabla \nabla \cdot) \boldsymbol{\pi}^{(n)}(\mathbf{r}) \quad (2)$$

$$\mathbf{H}^{(n)}(\mathbf{r}) = i\omega\epsilon_n \nabla \times \boldsymbol{\pi}^{(n)}(\mathbf{r}) \quad (3)$$

where $k_n = \omega\sqrt{\mu_n\epsilon_n}$ and $\boldsymbol{\pi}^{(n)}(\mathbf{r})$ are the wavenumber and electric Hertzian potential in region n , respectively. Assuming that the current source is in region 1, then

$$\begin{aligned} \boldsymbol{\pi}^{(1)}(\mathbf{r}) &= \boldsymbol{\pi}_1^p(\mathbf{r}) + \boldsymbol{\pi}_1^s(\mathbf{r}) \\ &= \int_{\Omega} \{ \underline{\mathbf{g}}^p(\mathbf{r}, \mathbf{r}') + \underline{\mathbf{g}}^r(\mathbf{r}, \mathbf{r}') \} \cdot \frac{\mathbf{J}^{(1)}(\mathbf{r}')}{i\omega\epsilon_1} d\Omega' \\ \boldsymbol{\pi}^{(2)}(\mathbf{r}) &= \boldsymbol{\pi}_2^s(\mathbf{r}) = \int_{\Omega} \underline{\mathbf{g}}^t(\mathbf{r}, \mathbf{r}') \cdot \frac{\mathbf{J}^{(1)}(\mathbf{r}')}{i\omega\epsilon_1} d\Omega' \end{aligned} \quad (4)$$

where the underscore indicates a dyadic quantity, and where Ω is the support of the current. With y parallel to the interface normal, the principle Green dyadic can be written as

$$\begin{aligned} \underline{\mathbf{g}}^p(\mathbf{r}, \mathbf{r}') &= \mathbf{I} \frac{e^{-ik_1 R}}{4\pi R} \\ &= \mathbf{I} \frac{1}{(2\pi)^2} \int_{-\infty}^{\infty} \int_{-\infty}^{\infty} \frac{e^{-p_1|y-y'|}}{2p_1} e^{-i\mathbf{q}\cdot(\mathbf{r}-\mathbf{r}')} dq_x dq_y \end{aligned} \quad (5)$$

where $\mathbf{q} = \hat{\mathbf{x}}q_x + \hat{\mathbf{z}}q_z$, $k_\rho = |\mathbf{q}| = \sqrt{q_x^2 + q_z^2}$, $p_n^2 = q_\rho^2 - k_n^2$, $\rho = \sqrt{(x-x')^2 + (z-z')^2}$, $R = |\mathbf{r}-\mathbf{r}'| = \sqrt{\rho^2 + (y-y')^2}$ and \mathbf{I} is the unit dyadic.

The scattered Green dyadics can be obtained by enforcing the boundary conditions

$$\begin{aligned} \hat{\mathbf{z}} \times (\mathbf{H}_1 - \mathbf{H}_2) &= \mathbf{J}_e^s \\ \hat{\mathbf{z}} \times (\mathbf{E}_1 - \mathbf{E}_2) &= -\mathbf{J}_m^s \end{aligned} \quad (6)$$

where \mathbf{J}_e^s (A/m) and \mathbf{J}_m^s (V/m) are electric and magnetic surface currents on the boundary. In our case, $\mathbf{J}_m^s = \mathbf{0}$, and $\mathbf{J}_e^s = \underline{\sigma} \cdot \mathbf{E}$. Introducing the two-dimensional Fourier transform

$$\mathbf{a}(\mathbf{q}, y) = \int_{-\infty}^{\infty} \int_{-\infty}^{\infty} \mathbf{a}(\mathbf{r}) e^{i\mathbf{q}\cdot\mathbf{r}} dx dz \quad (7)$$

$$\mathbf{a}(\mathbf{r}) = \frac{1}{(2\pi)^2} \int_{-\infty}^{\infty} \int_{-\infty}^{\infty} \mathbf{a}(\mathbf{q}, y) e^{-i\mathbf{q}\cdot\mathbf{r}} dq_x dq_z \quad (8)$$

and enforcing the boundary conditions, the scattered Green dyadic is found to have the form

$$\underline{\mathbf{g}}^{r,t} = \begin{pmatrix} g_{xx}^{r,t} & g_{xy}^{r,t} & 0 \\ g_{yx}^{r,t} & g_{yy}^{r,t} & g_{yz}^{r,t} \\ 0 & g_{zy}^{r,t} & g_{zz}^{r,t} \end{pmatrix} \quad (9)$$

where the Sommerfeld integrals are

$$\begin{aligned} g_{\alpha\beta}^r(\mathbf{r}, \mathbf{r}') &= \\ \frac{1}{(2\pi)^2} \int_{-\infty}^{\infty} \int_{-\infty}^{\infty} w_{\alpha\beta}^r(q_x, q_z) \frac{e^{-p_1(y+y')}}{2p_1} e^{-i\mathbf{q}\cdot(\mathbf{r}-\mathbf{r}')} dq_x dq_z \end{aligned} \quad (10)$$

The Green dyadic for region 2, $\underline{\mathbf{g}}^t(\mathbf{r}, \mathbf{r}')$, has the same form as for region 1, although in (10) the replacement $w_{\alpha\beta}^r e^{-p_1(y+y')} \rightarrow w_{\alpha\beta}^t e^{p_2 y} e^{-p_1 y'}$ must be made.

The coefficients $w_{\alpha\beta}^{r,t}$ are complicated for the inhomogeneous case, and in the following we assume the sheet is in a homogeneous space $\epsilon_2 = \epsilon_1 = \epsilon$, $\mu_2 = \mu_1 = \mu$ and $w_{\alpha\beta}^r = N_{\alpha\beta}(q_x, q_z)/D(q_x, q_z)$,

$$\begin{aligned} D(q_x, q_z) &= 2\sigma_{xx}(k^2 - q_x^2) + 2\sigma_{zz}(k^2 - q_z^2) \\ &\quad - i4\frac{k}{\eta} p \left(1 + \frac{1}{4}\eta^2 \sigma_{xx} \sigma_{zz} \right), \end{aligned} \quad (11)$$

and

$$\begin{aligned} N_{yy}(q_x, q_z) &= -p^2(\sigma_{xx} + \sigma_{zz}) - ipk\eta\sigma_{xx}\sigma_{zz}, \\ N_{xy}(q_x, q_z) &= iq_x p(\sigma_{xx} - \sigma_{zz}), \\ N_{zy}(q_x, q_z) &= -iq_z p(\sigma_{xx} - \sigma_{zz}), \end{aligned} \quad (12)$$

where $p = \sqrt{q_x^2 + q_z^2 - k^2}$, and $\eta = \sqrt{\mu/\epsilon}$. Finally, we have, e.g.,

$$E_y = \frac{1}{j\omega\epsilon} \left(k^2 + \frac{\partial^2}{\partial y^2} \right) (g_{yy}^p(\mathbf{r}, \mathbf{r}') + g_{yy}^r(\mathbf{r}, \mathbf{r}')) + \frac{\partial^2}{\partial x \partial y} g_{xy}^r(\mathbf{r}, \mathbf{r}') + \frac{\partial^2}{\partial z \partial y} g_{zy}^r(\mathbf{r}, \mathbf{r}') \quad (13)$$

and other field components are obtained from (2).

A. Complex-Plane Analysis in the q_x -Plane

In the case of an isotropic material the coefficients $w_{\alpha\beta}$ only depend on $q^2 = q_x^2 + q_z^2$, leading to

$$g_{\alpha\beta}^r(\mathbf{r}, \mathbf{r}') = \frac{1}{2\pi} \int_0^\infty w_{\alpha\beta}(q) \frac{e^{-p(y+y')}}{2p} J_0(q\rho) q dq \\ = \frac{1}{2\pi} \int_{-\infty}^\infty w_{\alpha\beta}(q) \frac{e^{-p(y+y')}}{4p} H_0^{(2)}(q\rho) q dq \quad (14)$$

where J_0 and $H_0^{(2)}$ are the usual zeroth-order Bessel and Hankel functions, respectively. In this case, such as occurs for graphene without a magnetic bias, the pole of $w_{\alpha\beta}$ leads to a simple analytical form for the SPP field [12]. However, this is not the case for an anisotropic material. Since the two-dimensional Sommerfeld integral can be time-consuming to evaluate, writing

$$g_{\alpha\beta}^r(\mathbf{r}, \mathbf{r}') = \frac{1}{(2\pi)} \int_{-\infty}^\infty dq_z e^{-iq_z(z-z')} f_{\alpha\beta}(q_z) \quad (15)$$

where

$$f_{\alpha\beta}(q_z) = \frac{1}{(2\pi)} \int_{-\infty}^\infty w_{\alpha\beta}(q_x, q_z) \frac{e^{-p(y+y')}}{2p} e^{-iq_x(x-x')} dq_x \quad (16)$$

the "inner" integral $f_{\alpha\beta}(q_z)$ can be evaluated as an SPP residue term (discrete spectral component) and branch cut integral representing the radiation continuum into space (note that the choice of "inner" and "outer" integrals is arbitrary). The branch cut in the q_x plane is the usual hyperbolic branch cut associated with the branch point due to $p = \sqrt{q_x^2 + q_z^2 - k^2}$, occurring at $q_x = \pm\sqrt{q_z^2 - k^2}$ [36]. Then,

$$f_{\alpha\beta}(q_z) = -iw'_{\alpha\beta}(q_{xp}, q_z) \frac{e^{-p(q_{xp})(y+y')}}{2p(q_{xp})} e^{-iq_{xp}(x-x')} \\ + \frac{1}{2\pi} \int_{bc} w_{\alpha\beta}(q_x, q_z) \frac{e^{-p_1(y+y')}}{2p_1} e^{-iq_x(x-x')} dq_x \quad (17)$$

where the first term is the residue contribution and bc indicates the hyperbolic branch-cut contour. In (17), $w'(q_{xp}, q_z) = N(q_{xp}, q_z)/D'(q_{xp}, q_z)$, $D'(q_x, q_z) = \frac{d}{dq_x} D(q_x, q_z)$, and where q_{xp} is the root of $D(q_x, q_z) = 0$ for a given q_z ,

$$q_{xp}(q_z) = \pm \sqrt{\frac{-B \pm \sqrt{B^2 - 4AC}}{2A}} \quad (18)$$

where $A = \sigma_{xx}^2$, $B = \frac{1}{4}\alpha^2 - 2k^2\sigma_{xx}^2 + 2(q_z^2 - k^2)\sigma_{xx}\sigma_{zz}$, $C = k^4(\sigma_{xx} + \sigma_{zz})^2 + q_z^2(q_z^2 - 2k^2)\sigma_{zz}^2 - 2k^2q_z^2\sigma_{xx}\sigma_{zz} + \frac{1}{4}\alpha^2(q_z^2 - k^2)$, and $\alpha = (4k/\eta)(1 + \frac{1}{4}\eta^2\sigma_{xx}\sigma_{zz})$.

For the SPP field of interest here (i.e., close to the interface, $(y, y' \ll \lambda)$) the branch cut term can be ignored and the residue term suffices for the calculation of $f(q_z)$,

$$f_{\alpha\beta}^{\text{SPP}}(q_z) \approx -iw'_{\alpha\beta}(q_{xp}, q_z) \frac{e^{-p(q_{xp})(y+y')}}{2p(q_{xp})} e^{-iq_{xp}(x-x')}, \quad (19)$$

which considerably speeds up evaluation of the Green function (rendering it one-dimensional). Since q_{xp} is the propagation constant along the x -axis, the \mp outside the square root in (18) indicates forward/backward propagation, whereas the inner \pm sign choice governs propagation of different modes (only one of which will propagate). Assuming $(x - x_0) > 0$, the term $e^{-iq_{xp}(x-x_0)}$ necessitates that $\text{Im}(q_{xp}) < 0$ to have a decaying wave traveling away from the source along the x -axis.

As an example, we consider an anisotropic surface with $\sigma_{xx} = 0.02 + 0.57i$ mS and $\sigma_{zz} = 0.02 - 0.57i$ mS. As discussed in Appendix A, such a conductivity tensor can be physically realized by an array of densely packed graphene strips at terahertz and near infrared frequencies. Fig. 2 compares $f_{yy}(q_z)$ obtained numerically by performing the integral (16) and obtained by using the residue term only, (19). The source is located at $y = \lambda/50$, very near the surface, and radiating at frequency 10 THz. Although not shown, for source or observation points relatively far from the surface, the branch cut integral is important, and can be the dominant contribution to the scattered field.

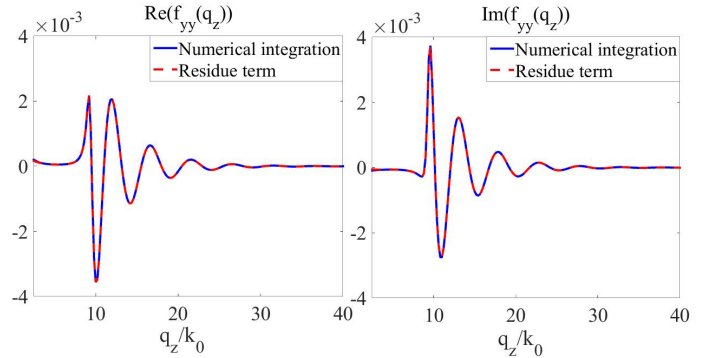


Fig. 2. Real and imaginary parts of $f_{yy}(q_z)$ obtained numerically, (16), and using the residue term (19) for an array of graphene strips at $f = 10$ THz. The source is $\lambda/50$ above the surface, and $x = 0.2\lambda$.

In the following we are interested in materials that provide a strong reactive and low-loss response, $\text{Im}(\sigma_{\alpha\alpha}) \gg \text{Re}(\sigma_{\alpha\alpha})$. In addition, the absolute size of $\text{Im}(\sigma_{\alpha\alpha})$ is important [43]. The ability of a surface to support a strong SPP depends on the ratio of the branch cut term (space radiation spectra) to the residue (SPP) term in the inner integral (17). In Fig. 3 we assume a general hyperbolic form $\sigma_{xx} = \alpha\sigma_0(0.01 + i)$ and $\sigma_{zz} = 0.1\sigma_{xx}^*$ where $\sigma_0 = e^2/4\hbar$ is the conductance quantum, e is the electron charge, and $*$ indicates complex conjugation. We assume that losses are relatively small, and use α in order to vary the magnitude of the conductivity.

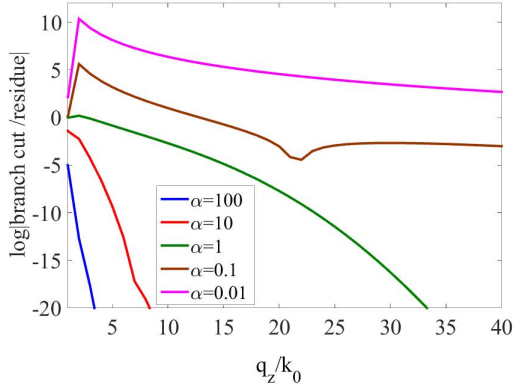


Fig. 3. Ratio of the branch cut and residue terms in (17), $s_{xx} = \alpha\sigma_0(0.01 + i)$, $\sigma_{zz} = 0.1\sigma_{xx}^*$, $\sigma_0 = e^2/4\hbar$. Source is positioned $\lambda/50$ above the surface, $f = 10$ THz, and $x = 0.2\lambda$.

It is clearly shown that for conductivity values smaller than the conductance quantum, the radiation spectra is dominant (in the limit that $|\sigma| \rightarrow 0$, the surface vanishes and the entire response is the radiation continuum produced by a source in free space). We have found that conductivity values on the order of the conductance quantum are somewhat borderline; an SPP can exist, although it may not be strongly dominant over the branch cut continuum for small q_z . Conductivities an order of magnitude or more above the conductance quantum provide a very strong SPP response in which the branch cut contribution is negligible except exceedingly close to the source.

For large q_z , (18) becomes

$$q_{xp}(q_z) = q_z \sqrt{-\frac{\sigma_{zz}}{\sigma_{xx}}} \quad (20)$$

The SPP direction of propagation on the 2D anisotropic surface is easily determined as $\tan^{-1}(\frac{q_{xp}}{q_z})$, and using (20) the angle of propagation with respect to the x -axis is simply

$$\phi = \tan^{-1} \sqrt{-\frac{\sigma_{zz}}{\sigma_{xx}}}. \quad (21)$$

Therefore in the anisotropic hyperbolic case the SPP is directed along a specific angle. For the isotropic case ($\sigma_{xx} = \sigma_{zz}$) this does not occur, since $q_{xp}^2 + q_z^2 = q_p^2$ where q_p is a constant. If we measure the angle ϕ relative to the positive x -axis then at each point in the plane of the material we have $x = \rho \cos \phi$, $z = \rho \sin \phi$, $q_{xp} = q_p \cos \phi$ and $q_z = q_p \sin \phi$. If the source is at the origin then we have

$$e^{-i\mathbf{q}\cdot(\mathbf{r}-\mathbf{r}')} = e^{-i(q_{xp}x+q_zz)} = e^{-i\Gamma\rho(\cos^2\phi+\sin^2\phi)} = e^{-i\Gamma\rho} \quad (22)$$

which describes a SPP wave that is radially propagating along all directions in the plane of the surface. However, in the anisotropic case for large q_z ,

$$\begin{aligned} e^{-i\mathbf{q}\cdot(\mathbf{r}-\mathbf{r}')} &= e^{-i(q_{xp}x+q_zz)} = e^{-i(q_z\sqrt{-\frac{\sigma_{zz}}{\sigma_{xx}}}x+q_zz)} \\ &= e^{-iq_z\rho(\sqrt{-\frac{\sigma_{zz}}{\sigma_{xx}}}\cos\phi+q_z\sin\phi)} \end{aligned} \quad (23)$$

and the maximum of $(\sqrt{-\frac{\sigma_{zz}}{\sigma_{xx}}}\cos\phi+q_z\sin\phi)$ determines the angle at which the SPP is directed. It can be simply shown that this angle is (21). This leads to the conclusion that hyperbolic anisotropy, in contrast to the isotropic case, results in a directed SPP, as expected.

As a function of $\underline{\sigma}$, there are different dispersion scenarios for SPP propagation. The usual elliptic case is obtained when both imaginary parts of the conductivity have the same sign (inductive when $\text{Im}(\sigma_{xx,zz}) < 0$, capacitive otherwise). A graphene sheet with dominant intra-band conductivity term with $\text{Im}(\sigma_{xx}) = \text{Im}(\sigma_{zz}) < 0$ is a natural example of an elliptic isotropic sheet that can support a TM omni-directional SPP. The hyperbolic case occurs when the sign of the imaginary parts of the conductivity components are different. As discussed in Appendices A and C, both a graphene strip metasurface (potentially, metal strips as well) and natural black phosphorus can provide a hyperbolic 2D surface. In this case, as shown in (21) and (23), energy propagation is focused along specific directions governed by the conductivity components [3].

III. COMPLEX-PLANE ANALYSIS IN THE $q_z - \text{Plane}$

Although the SPP field can be evaluated from a one-dimensional numerical integral, (16) with (19), it is useful to consider complex-plane analysis of the “outer” integral over q_z . Branch-point singularities of the complex function $f_{\alpha\beta}^{\text{SPP}}(q_z)$, (19), the residue term of the q_x integral, are described next; there are no poles. Regarding the two complex planes $q_x - q_z$, a sufficient condition in order to have a branch point in the $q_z - \text{plane}$ is that

$$D(q_x, q_z) = \frac{d}{dq_x} D(q_x, q_z) = 0 \quad (24)$$

with $\delta = \frac{d}{dq_z} D(q_x, q_z) \frac{d^2}{dq_z^2} D(q_x, q_z) \neq 0$ [37] (note that although (24) represents a second-order zero of D , these points are not necessarily branch points without the condition $\delta \neq 0$). These branch points are associated with modes in the q_x -plane merging at a certain value of q_z , forming a second-order zero of D . Another possible branch point in the q_z plane is associated with the square-root in p . The fact that a pole in one spectral plane results in a branch point in another spectral plane was recognized in studies of microstrip and other integrated waveguides [32]-[35].

A. p-type branch point in the $q_z - \text{plane}$

For the isotropic case, $p = \sqrt{q^2 - k^2}$ and the p-type branch point occurs at $q = \pm k$, resulting in the usual hyperbolic branch cuts in the q -plane [36]. In this case, $q_x^2 + q_z^2 = q_p^2$ is a constant and $q_z = \sqrt{k^2 - q_x^2}$ leads to branch points at $q_x = \pm k$. However, for the residue, $q_p^2 = q_{xp}^2(q_z) + q_z^2$ is a constant in q_z and so we never have $q_p = k$ for any q_z , and so there is no p-type BP in the $q_z - \text{plane}$ for the SPP for the

isotropic case. However, for anisotropic media $q_{xp}^2(q_z) + q_z^2$ is not generally a constant, and so there can be a “p-type” BP in the q_z -plane, where $p = \sqrt{q_{xp}^2(q_z) + q_z^2 - k^2} = 0$, although this will not occur at $q_z = k$ unless $q_{xp}(k) = 0$. In any event, since this branch cut relates to radiation into space, for the SPP we can ignore this contribution to the SPP field.

B. Type-0 branch point in the q_z -plane

Introducing the notation that $(q_x^{(n)}, q_z^{(n)})$ represents the pair of spectral values that satisfy the conditions for a branch point/pole pair, (24) and $\delta \neq 0$, since the residue term already satisfies $D(q_{xp}, q_z) = 0$, we can find branch points in the q_z -plane from $\frac{d}{dq_x} D(q_{xp}(q_z), q_z) = 0$,

$$\left(\sigma_{xx} + \frac{ik/\eta}{\sqrt{q_{xp}^2 + q_z^2 - k^2}} \left(1 + \frac{1}{4}\eta^2 \sigma_{xx} \sigma_{zz} \right) \right) q_{xp}(q_z) = 0. \quad (25)$$

As we will show later, these branch points have a significant role in the analysis of the SPP. Because of their importance, we categorize them into two groups, type-0 and type-1 branch points.

First we define type-0 branch points as those values of q_z for which $q_{xp}(q_z) = 0$ in (25); i.e., the merging of the forward and backward modes (associated with different signs in the outer square-root in (18)) in the q_x -plane at a certain value of q_z [37], given by

$$q^{(+0)} = q_z^{\text{TM}} = k \sqrt{1 - \left(\frac{2}{\eta \sigma_{zz}} \right)^2} \quad (26)$$

$$q^{(-0)} = q_z^{\text{TE}} = k \sqrt{1 - \left(\frac{\eta \sigma_{xx}}{2} \right)^2} \quad (27)$$

such that the pair $(q_x, q_z) = (0, q^{\text{TM/TE}})$ form a pole-branch-point pair. For $\sigma_{xx} = \sigma_{zz}$ these are well-known TM and TE SPP wavenumbers, respectively. Graphene is an example of such a 2D isotropic layer which can support these modes [12].

C. Type-1 branch point in the q_z -plane

Another set of singularities in the q_x - q_z plane is related to the point in the q_z -plane where modes q_{xp} associated with different signs in the inner square-root in (18) merge for $q_{xp} \neq 0$. These can be obtained by simultaneously solving the equations $D(q_x, q_z) = 0$ and $\frac{dD(q_x, q_z)}{dq_x} = 0$, leading to

$$q_x^{(\pm 1)} = \sqrt{\frac{-k^2}{\delta \sigma} \left(\sigma_{xx} + (\sigma_{zz} \mp 2\sigma_{xx}) \frac{(1 + \frac{1}{4}\eta^2 \sigma_{xx} \sigma_{zz})^2}{\eta^2 \sigma_{xx}^2} \right)} \quad (28)$$

$$q_z^{(\pm 1)} = \sqrt{-(q_x^{(\pm 1)})^2 + k^2 \left(1 - \frac{(1 + \frac{1}{4}\eta^2 \sigma_{xx} \sigma_{zz})^2}{\eta^2 \sigma_{xx}^2} \right)} \quad (29)$$

where $\delta \sigma = \sigma_{zz} - \sigma_{xx}$, such that $(q_x, q_z) = (q_x^{(\pm 1)}, q_z^{(\pm 1)})$ form a pole-branch-point pair.

D. Branch cut analysis in the q_z -plane

Using the SPP field (19) and performing the outer integration, the Green function is

$$g_{\alpha\beta}^r = \frac{-i}{2\pi} \int_{-\infty}^{+\infty} w'_{\alpha\beta}(q_{xp}, q_z) \frac{e^{-p(y+y')}}{2p} e^{-iq_{xp}(x-x')} \times e^{-iq_z(z-z')} dq_z. \quad (30)$$

Assuming $(z-z') > 0$, due to the term $e^{-iq_z(z-z')}$ the contour can be closed in the lower half plane of the q_z -plane, leading to

$$g_{\alpha\beta}^r \approx \frac{-i}{2\pi} \int_{\text{bc}} w'_{\alpha\beta}(q_{xp}, q_z) \frac{e^{-p(y+y')}}{2p} e^{-iq_{xp}(x-x')} \times e^{-iq_z(z-z')} dq_z \quad (31)$$

where the branch cut integral is over all branch cuts. Also, from the term $e^{-iq_{xp}(x-x')}$ it is clear that for $x-x' \geq 0$ than only when $\text{Im}(q_{xp}) \leq 0$ do we obtain an SPP that decays away from the source. Therefore, we have in the q_z -plane two Riemann sheets, the top (proper) sheet where $\text{Im}(q_{xp}) \leq 0$ and the bottom sheet where $\text{Im}(q_{xp}) \geq 0$, for $x-x' \geq 0$. Those values of q_z that leads to $\text{Im}(q_{xp}) = 0$ determine the branch cut trajectory which separates the proper from improper Riemann sheets (again, we ignore the branch cut associated with p , which introduces another two sheets; we enforce $\text{Re}(p) > 0$).

Typically, branch cut trajectories to separate certain Riemann sheets can be analytically determined from the functional dependence of the multi-valued function that defines the branch point. However, for anisotropic surfaces the form of q_{xp} is too complicated to determine a simple equation for the branch cut for $\text{Im}(q_{xp}) = 0$. As an example, Fig. 4-a shows the branch cuts for $\text{Im}(q_{xp}) = 0$ obtained by plotting $\text{Im}(q_{xp})$ for an array of graphene strips (see Appendix A) in the hypothetical lossless case (i.e., ignoring the real parts of the conductivities) at 10 THz. Fig. 4-b shows a close-up near the Im axis, and Fig. 4-c shows the properly-cut q_z -plane for the lossless case. It can be seen that for the considered frequency the TM branch point leads to a branch cut starting at q_z^{TM} and going horizontally to infinity, and the TE branch point q_z^{TE} and the branch point $q_z^{(-1)}$ are connected by a branch cut. The branch point $q_z^{(+1)}$ is on the improper Riemann sheet (not shown).

Insight into the correct branch cut can be obtained from a large q_z approximation. From (20), for a lossy material $\sigma_{xx} = \sigma'_{xx} + i\sigma''_{xx}$ and $\sigma_{zz} = \sigma'_{zz} + i\sigma''_{zz}$ then the branch cut trajectory is along q_z values such that

$$\text{Im}(iq_z \sqrt{\sigma'_{zz}\sigma'_{xx} + i\sigma''_{zz}\sigma'_{xx} - i\sigma'_{xx}\sigma''_{zz} + \sigma''_{xx}\sigma''_{zz}}) = 0. \quad (32)$$

For a lossless surface, $\sigma'_{xx} = \sigma'_{zz} = 0$, leading to

$$\text{Im}(iq_z \sqrt{\sigma''_{xx}\sigma''_{zz}}) = 0, \quad (33)$$

such that if $\sigma''_{xx}\sigma''_{zz} > 0$ the BC is along $\text{Im}(q_z)$, and if $\sigma''_{xx}\sigma''_{zz} < 0$ the BC is along $\text{Re}(q_z)$, in agreement with the numerically-determined contours.

The branch cut integrals can be viewed as a continuous superposition of modes. The BP q_z^{TM} is associated with the pair $(q_x, q_z) = (0, q_z^{\text{TE}}) = (0, 9.3)k_0$ for the numerical example considered, and along the branch cut, as $\text{Re}(q_x) = \text{Re}(q_{xp})$ also increases from zero, and the resulting continuum summation of pair values synthesis the beam. Similar comments apply to the branch cut between q_z^{TE} and q_z^{-1} (between $q_z = 1.005k_0$ and $-3.22ik_0$ in the numerical example considered).

The lossy case is shown in Fig. 5; the branch cut trajectory deflects a bit from the lossless case, but for low-loss material the lossless BC contour is sufficient.

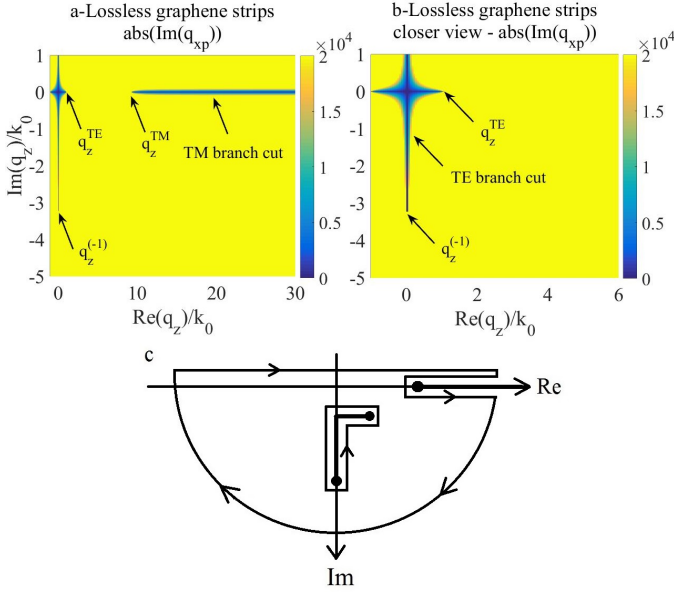


Fig. 4. a,b: Branch cut contours $\text{Im}(q_{xp}) = 0$ determined from a plot of the absolute value of $\text{Im}(q_{xp})$ for a lossless model of a graphene strip array at 71.8 THz ($\sigma'_{xx} = \sigma'_{zz} = 0$, $\sigma''_{xx} = 0.57i$ mS, $\sigma''_{zz} = -0.57i$ mS). The branch point locations are $q_z^{\text{TE}}/k_0 = 1.005$, $q_z^{\text{TM}}/k_0 = 9.22$, $q_z^{(-1)}/k_0 = -3.22i$. c. Integration contour in the q_z -plane showing branch points (dots) and branch cuts (thick lines).

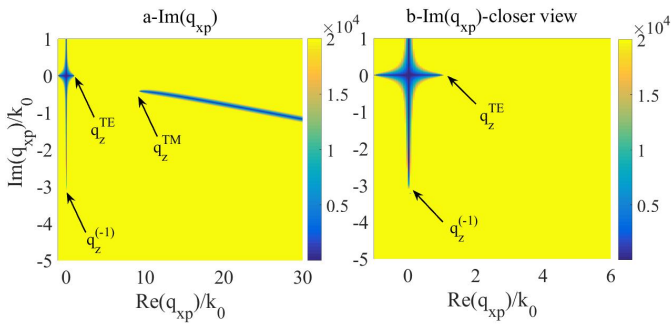


Fig. 5. Branch cut contours $\text{Im}(q_{xp}) = 0$ determined from a plot of the absolute value of $\text{Im}(q_{xp})$ for a lossy model of a graphene strip array at 10 THz with $\sigma_{xx} = 0.02 + 0.57i$ mS and $\sigma_{zz} = 0.02 - 0.57i$ mS.

As a common special case, for an inductive isotropic surface such as graphene in the far-infrared,

$$\sigma_{xx} = \sigma_{zz} = \frac{-ie^2 k_B T}{\pi \hbar^2 (\omega - i2\Gamma)} \times \left(\frac{\mu_c}{k_B T} + 2 \ln \left(1 + e^{-\frac{\mu_c}{k_B T}} \right) \right). \quad (34)$$

Here we consider graphene at $T = 300$ K, $\mu_c = 0.5$ eV and $f = 20$ THz. In this case the TE related branch point is at $q_z^{\text{TE}} = k(1.0039 + 0.0001i)$, and so is not implicated in the lower-half-plane closure, consistent with the surface being inductive. The TM related BP occurs at $q_z^{\text{TM}}/k_0 = (11.3706 - 0.2088i)$. The two other type-1 branch points move to infinity as the material becomes isotropic, and therefore the branch cut extends down the entire imaginary axis (therefore for both the isotropic and anisotropic cases there is a branch cut between q_z^{TM} and q_z^{-1}). Fig. 6 shows a surface plot of $\text{Im}(q_{xp})$ in the q_z -plane.

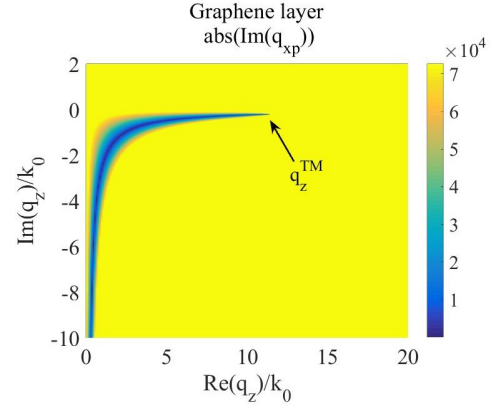


Fig. 6. Branch cut contour $\text{Im}(q_{xp}) = 0$ determined from a plot of the absolute value of $\text{Im}(q_{xp})$ for graphene with $\mu_c = 0.5$ eV at $T = 0$ K and $f = 20$ THz.

For isotropic and inductive graphene only a TM mode can propagate, and so the contribution is from the TM-related branch point and associated cut, as expected. For the graphene strip array anisotropic case, the hybrid nature of the modes supported by such a surface involve both TE and TM-related branch points, and, in contrast to the isotropic case, three branch points contribute to the field.

E. Conductivity and its effect on branch points and SPP confinement

Analytically it can be shown that both type-1 branch points $q_z^{(\pm 1)}$ can be connected to a TE or TM branch point, depending on the conductivity value. Two cases are of particular interest, small conductivity values, $(\eta\sigma_{xx/zz})^2/2 \ll 1$, and large conductivity values, $(\eta\sigma_{xx/zz})^2/2 \gg 1$. For small conductivity values, from (26)-(27) we have

$$q_z^{\text{TM}} = k \sqrt{1 - \left(\frac{2}{\eta\sigma_{zz}} \right)^2} \rightarrow (\eta\sigma_{zz})^2 = \frac{4}{1 - \left(\frac{q_z^{\text{TM}}}{k} \right)^2} \quad (35)$$

$$q_z^{TE} = k \sqrt{1 - \left(\frac{\eta\sigma_{xx}}{2}\right)^2} \rightarrow \frac{1}{(\eta\sigma_{xx})^2} = \frac{1}{4} \frac{1}{1 - \left(\frac{q_z^{TE}}{k}\right)^2}. \quad (36)$$

Making these replacements in (28)-(29) and using the fact that for small conductivity like in our previous numeric example ($\sigma_{xx} = 0.02 + 0.57i$ mS and $\sigma_{zz} = 0.02 - 0.57i$ mS), $(\eta\sigma_{xx/zz})^2/2 \ll 1$, then $q_z^{TM} \gg k$ and $q_z^{TE} \approx k$, and so $(q_z^{TE})^2 \ll (q_z^{TM})^2$, such that

$$q_z^{(\pm 1)} = \frac{k}{2} \sqrt{\frac{1}{1 - \left(\frac{q_z^{TE}}{k}\right)^2} \frac{\sigma_{xx} \mp 2\sigma_{xx}}{\sigma_{zz} - \sigma_{xx}}}. \quad (37)$$

Therefore, for small values of σ_{xx} and σ_{zz} , the type-1 branch points are governed by (and associated with) the TE branch point q_z^{TE} .

For larger values of σ_{xx} and σ_{zz} the situation is different. In this case, for $(\eta\sigma_{xx/zz})^2/2 \gg 1$ we have $(q_z^{TM})^2 \ll (q_z^{TE})^2$ and it can be shown that an approximate expression for the type-1 branch point is (37) with q_z^{TM} replacing q_z^{TE} ; the type-1 branch points are associated with the TM related branch point. As the conductivity changes from a small to a large value, q_z^{TE} and q_z^{TM} move toward each other and then cross, and eventually interchange roles. Setting (26) and (27) equal to each other, it can be shown that these type-0 branch points meet at a frequency such that $\sigma_{xx}\sigma_{zz} = 4/\eta^2$.

As an example of a large conductivity situation, conductivity tensor components $\sigma_{xx} = 1.3 + 16.9i$ mS and $\sigma_{zz} = 0.4 - 9.2i$ mS are attainable using multi-layer graphene to form the strip array. For this set of conductivities the branch points and branch cuts are shown in Fig. 7. As can be seen, q_z^{TE} exceeds q_z^{TM} , there is a branch cut from q_z^{TE} to infinity, a branch cut between q_z^{TM} and q_z^{-1} , and q_z^{-1} is connected to q_z^{TM} .

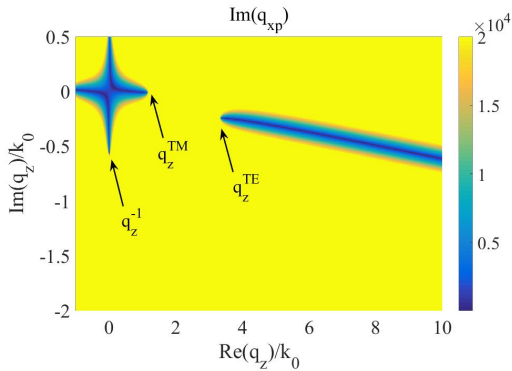


Fig. 7. Branch cut contours $\text{Im}(q_{xp}) = 0$ determined from a plot of the absolute value of $\text{Im}(q_{xp})$ for a lossy model of multi-layer graphene strip at 10 THz, $\sigma_{xx} = 1.3 + 16.9i$ mS and $\sigma_{zz} = 0.4 - 9.2i$ mS.

IV. DIRECTIVE SPPS ON HYPERBOLIC AND ANISOTROPIC SURFACES

A. Anisotropic hyperbolic layer (graphene strip array)

As shown in Appendix A, conductivity components $\sigma_{xx} = 0.02 + 0.57i$ mS and $\sigma_{zz} = 0.02 - 0.57i$ mS can be realized

using an array of graphene strips with $\mu_c = 0.33$ eV, strip width $W = 59$ nm, and period $L = 64$ nm. For this anisotropic hyperbolic surface, Fig. 8a shows the electric field E_y , the dominant field component, computed as a real-line integral (30), and as a sum of branch cut integrals (31); excellent agreement is found between the two methods (the branch cut integrals are faster to compute than the brute-force numerical integrals, but no attempt was made to optimize either integration). The branch cuts for this case are shown in Fig. 5. Figs. 8-b,c show similar agreement for different strip configurations as discussed below.

Although the direction of the beam is electronically controllable via the chemical potential, different combinations of physical parameters of the graphene strip array (width W and periodicity L) can also be used to produce a desired beam. An optimum geometry to produce a beam in a certain direction can be found by tuning all of these parameters simultaneously. As discussed in Appendix B, here we used a genetic algorithm (GA) to find the optimum set of electrical and geometrical parameters to produce a given beam angle. The geometry leading to the beam in Fig. 8-a was found in this manner, for a specified beam angle of 45 deg. Note the excellent agreement between desired and obtained beam angle. The chemical potential was then changed to produce the beam at 52 deg., for a fixed geometry. Thus, a significant aspect of using a graphene strip array is its electronic tunability by, e.g., varying the bias to control the chemical potential.

In Fig. 8-b a desired beam angle of 60 deg. was sought, and the GA was used to determine the optimized parameters; $\mu_c = 0.45$ eV, $W = 56.1$ nm and $L = 62.4$ nm, such that $\sigma_{xx} = 0.003 + 0.25i$ mS and $\sigma_{zz} = 0.03 - 0.76i$ mS, leading to the desired beam. Again, excellent agreement is found between the desired and final beam angles.

As a final example for the graphene strip array Fig. 8-c shows E_y for the case of multi-layer graphene strips (to increase the conductivity) as discussed in the previous section. By using five layers of graphene with $\mu_c = 1$ eV, $W = 196$ nm and $L = 200$ nm, the conductivities are $\sigma_{xx} = 1.3 + 16.9i$ mS and $\sigma_{zz} = 0.4 - 9.2i$ mS. The branch cuts are shown in Fig. 7. For this case, (21) indicates that the beam should be directed along $\phi = 36$ deg. Again, excellent agreement is found between the two methods and the position of the beam is along the desired angle.

B. Anisotropic non-hyperbolic layer (black phosphorus)

As discussed in Appendix C, black phosphorus is a natural material that can be used as a platform to realize an anisotropic surface. Although black phosphorus exhibits a hyperbolic regime, the resulting values of conductivity are rather small (to produce a hyperbolic response the interband conductivity must dominate one of the conductivity values (σ_{xx} or σ_{zz}), and the intraband conductivity must dominate the other component, resulting in the required sign difference). Although a hyperbolic SPP can be excited, the residue is not generally the dominant response. Therefore, in order to consider larger values of black phosphorus conductivity, we consider the non-hyperbolic (Drude) regime. A 10 nm thick

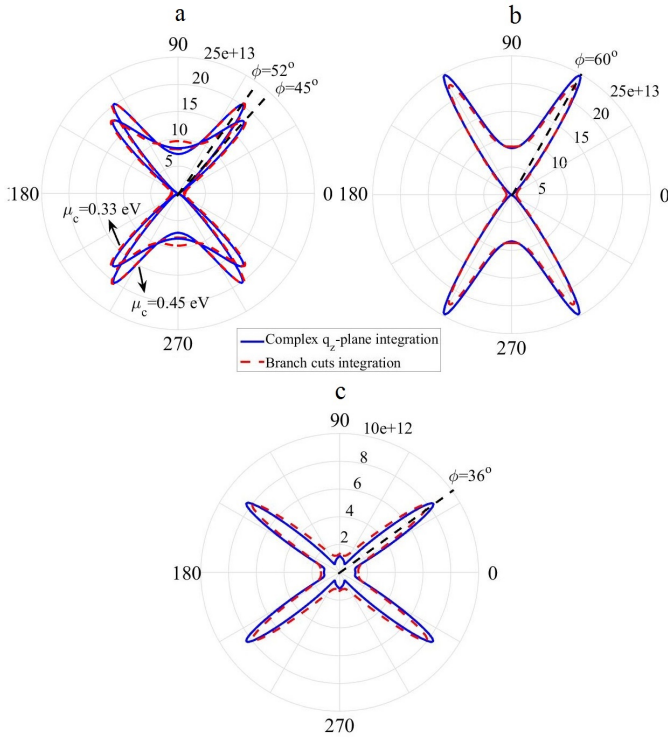


Fig. 8. Electric field E_y excited by a y -directed dipole current above a graphene strip array. a: graphene with $\mu_c = 0.45$ eV and $\mu_c = 0.33$ eV, $W = 59$ nm, $L = 64$ nm, $\sigma_{xx} = 0.02 + 0.57i$ mS and $\sigma_{zz} = 0.02 - 0.57i$ mS. b: $\mu_c = 0.45$ eV, $W = 56.1$ nm, $L = 62.4$ nm, $\sigma_{xx} = 0.003 + 0.25i$ mS and $\sigma_{zz} = 0.03 - 0.76i$ mS. c: Strip array with a 5-layer graphene, $\mu_c = 1$ eV, $W = 196$ nm and $L = 200$ nm, $\sigma_{xx} = 1.3 + 16.9i$ mS and $\sigma_{zz} = 0.4 - 9.2i$ mS. Blue line is for the integration along the real axis and dashed red line is for integration along the branch cuts.

black phosphorus film with doping level $10 \times 10^{13}/\text{cm}^2$ has conductivity tensor components $\sigma_{xx} = 0.0008 - 0.2923i$ mS and $\sigma_{zz} = 0.0002 - 0.0658i$ mS at $f = 92.6$ THz. Using (26), (27) and (29), a surface with these conductivity components has $q_z^{\text{TM}} = k(80.6804 - 0.2114i)$, $q_z^{\text{TE}} \approx k$, and $q_z^{(-1)} = k(-0.0300 - 10.3165i)$.

The imaginary components of the conductivities are negative, so that the surface is not able to support TE modes (the TE branch point is located at the upper half of the q_z -plane, and so not captured for $z - z' > 0$). The only active branch points are the TM related branch point and $q_z^{(-1)}$. Fig. 9-a shows the branch points and associated branch cuts in the q_z -plane. One important difference between branch cuts in this case and in the previous hyperbolic cases is the branch cut trajectory. From (33) for the hyperbolic case, because of the condition $\sigma_{xx}\sigma_{zz} < 0$ the branch cut trajectory was along the real axis, but for the anisotropic non-hyperbolic case we have $\sigma_{xx}\sigma_{zz} > 0$ and so the trajectory for large q_z is parallel to the imaginary axis.

As shown in Fig. 9-b, this anisotropic non-hyperbolic surface can support a directed SPP, although the beam is directed primarily along one of the coordinate axes. The electric field computed as a real-line integral (30) is in good agreement with the electric field obtained as a sum of branch cut integrals (31). Fig. 9-c shows the SPP field in logarithmic scale calculated by

numerically solving Maxwell's equations using a commercial finite-difference time-domain method (FDTD) from Lumerical solutions [38]. Good agreement with the results obtained by complex plane analysis is observed. Fig. 9-d shows the vertical variation of the beam in logarithmic scale calculated by Lumerical, showing strong SPP confinement to the surface. Using the Green function the attenuation length was found to be $p = 12\pi/\lambda$.

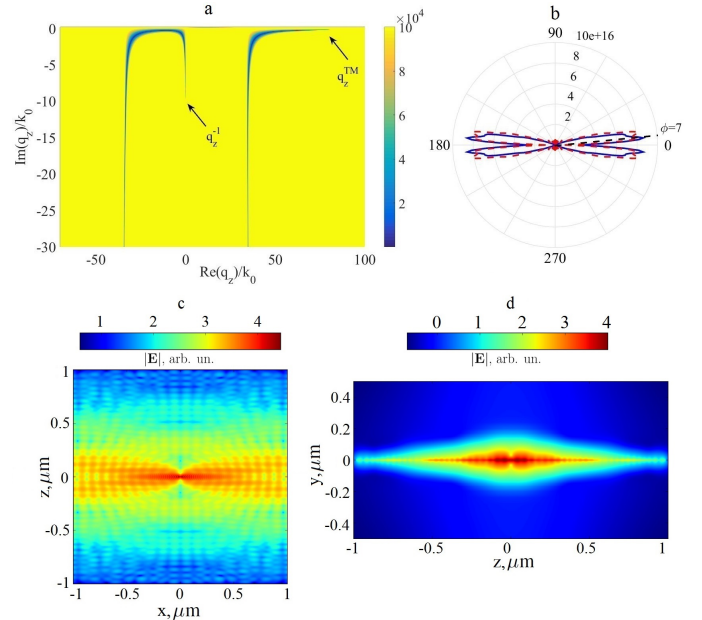


Fig. 9. a: Branch cut contours for $\text{Im}(q_{xp}) = 0$ determined from the absolute value of $\text{Im}(q_{xp})$ in the q_z -plane. b: Absolute value of E_y excited by a y -directed dipole current source above black phosphorus with doping level $10 \times 10^{13}/\text{cm}^2$ at $f = 92.6$ THz. The blue line is for the integration along the real axis and the dashed red line is for the integration along the branch cuts. c: SPP field in-plane distribution in logarithmic scale calculated by FDTD. d: SPP field vertical variation in logarithmic scale calculated by FDTD.

V. CONCLUSION

We have studied the electromagnetic response of two-dimensional anisotropic and hyperbolic surfaces and developed a method (based on complex plane analysis) for the efficient computation of electric field excited on such surfaces. A solution in term of electric field Sommerfeld integrals has been obtained for the electromagnetic field due to a vertical dipole current source located in close proximity to the surface. Poles, branch points, and related branch cuts and their relative importance and physical meaning for surface wave propagation has been emphasized. Examples have been shown for a graphene strip array and black phosphorus.

APPENDIX A

GRAPHENE STRIP HYPERBOLIC METASURFACE

A schematic of an array of graphene strips is shown in Fig. 10-a. This densely packed strip surface can act as a physical implementation of a metasurface at terahertz and near infrared frequencies [3], [39]. The dispersion topology of the proposed structure may range from elliptical to hyperbolic as

a function of its geometrical and electrical parameters. The in-plane effective conductivity tensor of the proposed structure can be analytically obtained using an effective medium theory as [3]

$$\sigma_{zz}^{\text{eff}} = \sigma \frac{W}{L} \quad \text{and} \quad \sigma_{xx}^{\text{eff}} = \frac{L\sigma\sigma_c}{W\sigma_c + G\sigma} \quad (38)$$

where L and W are the periodicity and width of the strips, respectively, $G = L - W$ is the separation distance between two consecutive strips, σ is graphene conductivity (34) and $\sigma_c = j \frac{\omega\epsilon_0 L}{\pi} \ln(\csc \frac{\pi G}{2L})$ is an equivalent conductivity associated with the near-field coupling between adjacent strips obtained using an electrostatic approach [40]. These effective parameters are valid only when the homogeneity condition $L \ll \lambda_{\text{SPP}}$ is satisfied, where λ_{SPP} is the plasmon wavelength in the in-plane direction perpendicular to the strips (x in this case), thus leading to a homogeneous 2D metasurface. Fig. 10-b and c shows σ_{xx} and σ_{zz} in a wide range of frequency for a graphene strip array with graphene parameters $\tau = 0.35$ ps, $\mu_c = 0.33$ eV, and geometrical parameters $W = 59$ nm and $L = 64$ nm. As can be seen from in Fig. 10-b, this structure can exhibit a hyperbolic response, as well as implement a non-hyperbolic although anisotropic surface.

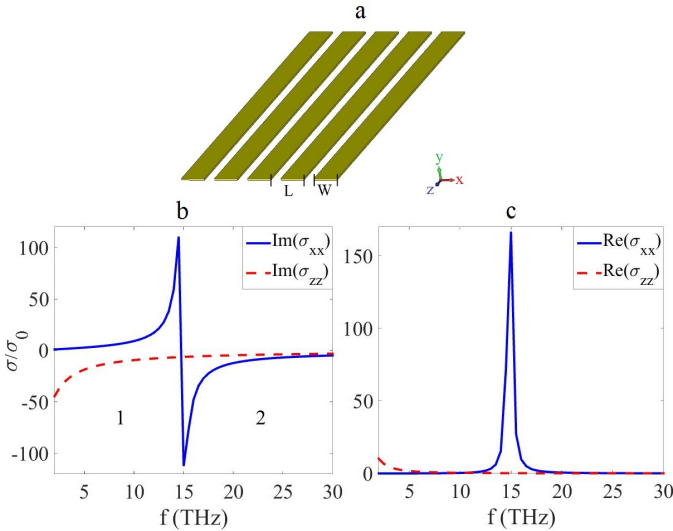


Fig. 10. a: Array of graphene strips. b: Imaginary parts of σ_{xx} and σ_{zz} and c: real parts of σ_{xx} and σ_{zz} normalized to $\sigma_0 = e^2/4h$ for a graphene strip array with $\tau = 0.35$ ps, $\mu_c = 0.33$ eV, $W = 59$ nm and $L = 64$ nm. Region 1 is hyperbolic and region 2 is simply anisotropic

APPENDIX B GENETIC ALGORITHM OPTIMIZATION

From (21), in the hyperbolic regime propagation along a desired direction can be obtained if the tensor conductivity components have the proper ratio. Designing a hyperbolic metasurface to produce a beam in a desired direction can be done by trial-and-error tuning of all geometrical and electrical parameters of the system, but a multi-variable optimization, such as a genetic algorithm (GA) is a good choice for this task.

The GA optimization is inspired by the biological process of genetics and evolution [41]. Genes are the basic building blocks of genetic algorithms, with each gene representing a parameter like width, periodicity or chemical potential. A chromosome is an array of genes, and each chromosome is passed under an evaluation process using a cost function assigning a relative merit to that chromosome. The algorithm begins with a large population of chromosomes found randomly from the search area of the parameters. Then, using a cost function, the fitness of each chromosomes is evaluated. The chromosomes are ranked from best to worst, and unacceptable chromosomes are discarded. Genes that survive become parents, by swapping some of their genetic material to produce two new offspring, and mutations cause small random changes in a chromosome. The offspring and the mutated chromosome are judged using the cost function, and the process is repeated. The algorithm stops after a set number of iterations, or when an acceptable solution is obtained [41]. Other optimization processes have the disadvantage of often getting stuck in local minima, but using a GA the mutation and the random nature of the process help to avoid this issue [42].

Here, we use an optimization code based on a GA to design an array of graphene strips that can support a SPP along a specific direction. As was stated, ideally the conductivity tensor elements of a hyperbolic metasurface should have large imaginary part and small real part, since such a surface can support a well-confined, long-range SPP. The cost function to be minimized was

$$\Psi(L, W, \mu_c, \phi) = \alpha(\text{Re}(\sigma_{xx}) + \text{Re}(\sigma_{zz})) + \frac{\beta}{|\text{Im}(\sigma_{xx})| + |\text{Im}(\sigma_{zz})|} + \gamma \left(\tan^2(\phi) + \frac{\sigma_{zz}}{\sigma_{xx}} \right) \quad (39)$$

where σ_{xx} and σ_{zz} are defined in (38). The cost function in (39) is a multi-objective cost function and the coefficients α , β and γ assign a weight (0 to 1) to each objective regarding to its importance. The first term in (39) assures a small real part of conductivity, the second term assures a large imaginary part, and the last term assures the correct ratio for σ_{zz} and σ_{xx} to obtain the SPP beam in a desired direction, where ϕ is the desired angle. It was found that $\alpha = 0.2$ and $\beta = \gamma = 0.4$ leads to good results, although the routine is relatively insensitive to these parameters.

APPENDIX C BLACK PHOSPHORUS

Black phosphorous is an anisotropic monolayer or thin-film material that can support surface plasmons [44]. Fig. 11 shows the in-plane conductivity tensor components at two doping levels, $10 \times 10^{13}/\text{cm}^2$ in Fig. 11-a and b and $5 \times 10^{12}/\text{cm}^2$ in Fig. 11-c and d, obtained from a Kubo formula as described in [23]. For a 10 nm BP film, the electronic band gap is approximately 0.5 eV. This accounts for the observed interband absorption along the x polarization, and also characterized by weak interband absorption along z .

It can be seen that by increasing the doping level, larger conductivity components are attainable but the hyperbolic

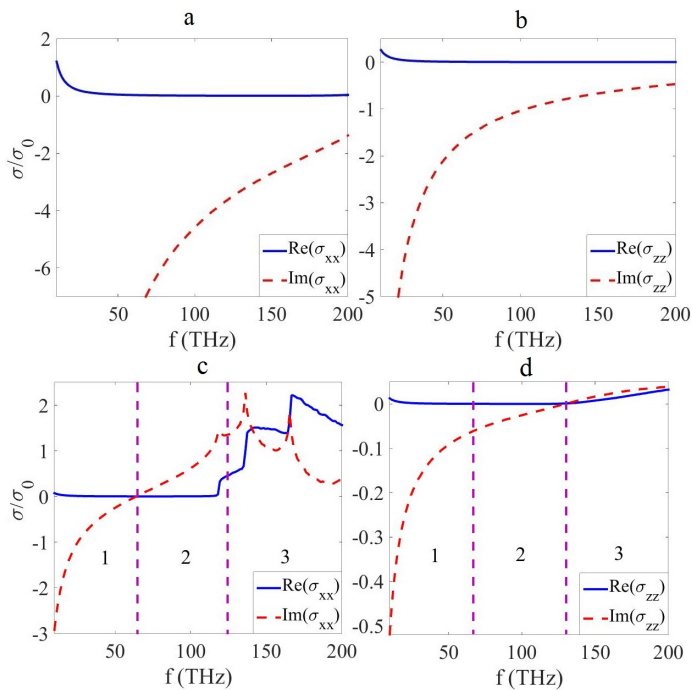


Fig. 11. a, b. Real and imaginary parts of σ_{xx} and σ_{zz} (x and z are in-plane crystal axes of BP, with x along the small effective mass direction, or commonly called the armchair direction) obtained at doping level $10 \times 10^{13}/\text{cm}^2$ and c,d. $5 \times 10^{12}/\text{cm}^2$ normalized to $\sigma_0 = e^2/4\hbar$ with a 10 nm thickness. Regions 1 and 3 show anisotropic inductive and capacitive responses, respectively, and region 2 shows the hyperbolic regime. $T=300$ K and damping is 2 meV.

region is also pushed toward higher frequencies. In Fig. 11-a and b black phosphorus is an inductive anisotropic (non-hyperbolic) surface while in Fig. 11-c and d regions 1 and 3 show anisotropic inductive and capacitive responses, respectively, and region 2 shows the anisotropic hyperbolic region.

ACKNOWLEDGMENT

TL was supported partially by the MRSEC Program of the National Science Foundation under Award Number DMR-1420013

REFERENCES

- [1] V. P. Drachev, V. A. Podolskiy, and A. V. Kildishev, *Hyperbolic metamaterials: new physics behind a classical problem*, Opt. Express 21, 15048 (2013).
- [2] LM. A. K. Othman, C. Guclu, and F. Capolino, *Graphene-based tunable hyperbolic metamaterials and enhanced near-field absorption*, Opt. Express 21, 7614 (2013).
- [3] J. Sebastian Gomez-Diaz, Mykhailo Tymchenko, and Andrea Al, *Hyperbolic plasmons and topological transitions over uniaxial metasurfaces*, PRL 114, 233901 (2015).
- [4] V. A. Podolskiy and E. E. Narimanov, *Strongly anisotropic waveguide as a nonmagnetic left-handed system*, Physical Review B, vol. 71, no. 20, pp. 14, 2005.
- [5] A. A. Goyadinov and V. A. Podolskiy, *Metamaterial photonic funnels for subdiffraction light compression and propagation*, Physical Review B, vol. 73, no. 15, Article ID 155108, pp. 15, 2006.
- [6] J. Yao, X. Yang, X. Yin, G. Bartal, and X. Zhang, *Threedimensional nanometer-scale optical cavities of indefinite medium* Proceedings of the National Academy of Sciences of the United States of America, vol. 108, no. 28, pp. 1132711331, 2011.

- [7] E. F. Kuester, M. A. Mohamed, M. Picket-May, and C. L. Holloway, *Averaged transition conditions for electromagnetic fields at a metafoil*, IEEE Trans. Antennas Propag. vol. 51, pp. 2641-2651, Oct. 2003.
- [8] Nanfang Yu, Federico Capasso, *Flat optics with designer metasurfaces*, Nature Materials 13, 139150 (2014).
- [9] Novoselov, K. S., D. Jiang, F. Schedin, T. J. Booth, V. V. Khotkevich, S. V. Morozov, and A. K. Geim. "Two-dimensional atomic crystals." Proceedings of the National Academy of Sciences of the United States of America 102, 10451-10453, no. 30 (2005).
- [10] T. Low and P. Avouris, *Graphene Plasmonics for Terahertz to Mid-Infrared Applications*, Acs. Nano 8, 1086 (2014).
- [11] F. H. L. Koppens, D. E. Chang, and F. J. Garca de Abajo, *Graphene plasmonics: a platform for Strong lightmatter interactions*, Nano Lett. 11, 3370 (2011).
- [12] G.W. Hanson, *Dyadic Greens functions and guided surface waves for a surface conductivity model of graphene*, J. Appl. Phys. 103, 064302 (2008).
- [13] F. Javier Garca de Abajo, *Graphene plasmonics: challenges and opportunities*, ACS Photonics 1, 135 (2014).
- [14] E. Forati, G.W. Hanson, A. B. Yakovlev, and A. Al, *Planar hyperlens based on a modulated graphene monolayer*, Phys. Rev. B 89, 081410 (2014).
- [15] George W. Hanson, S. A. Hassani Gangaraj, Changhyoung Lee, Dimitris G. Angelakis, Mark Tame, *Quantum plasmonic excitation in graphene and loss-insensitive propagation*, Phys. Rev. A 92, 013828, (2015).
- [16] D. L. Sounas, H. S. Skulason, H. V. Nguyen, A. Guermoune, M. Siaz, T. Szkopek, and C. Caloz, *Faraday rotation in magnetically biased graphene at microwave frequencies*, Appl. Phys. Lett. 102, 191901 (2013).
- [17] Vakil, Ashkan, and Nader Engheta. *Transformation optics using graphene*, Science 332, no. 6035 (2011): 1291-1294.
- [18] Morita. A, *Semiconducting black phosphorus*, Applied Physics A 39, no. 4 (1986): 227-242.
- [19] L.Li,Y.Yu,G.J.Ye,Q.Ge,X.Ou,H.Wu,D.Feng,X.H.Chen, Y. Zhang, *Black phosphorus field-effect transistors*, Nat. Nanotechnol. 9, 372 (2014).
- [20] H. Liu, A. T. Neal, Z. Zhu, D. Tomanek, P. D. Ye, *Phosphorene: an unexplored 2D semiconductor with a high hole mobility*, ACS Nano 8, 4033 (2014).
- [21] F. Xia, H. Wang, and Y. Jia, *Rediscovering black phosphorus as an anisotropic layered material for optoelectronics and electronics*, Nat. Commun. 5, 4458 (2014).
- [22] S. P. Koenig, R. A. Doganov, H. Schmidt, A. H. Neto, B. Oezylmaz, *Electric field effect in ultrathin black phosphorus*, Appl. Phys. Lett. 104, 103106 (2014).
- [23] Low, Tony, A. S. Rodin, A. Carvalho, Yongjin Jiang, Han Wang, Fengnian Xia, and AH Castro Neto, *Tunable optical properties of multilayer black phosphorus thin films*, Physical Review B 90, no. 7 (2014): 075434.
- [24] Tran, Vy, Ryan Soklaski, Yufeng Liang, and Li Yang, *Layer-controlled band gap and anisotropic excitons in few-layer black phosphorus*, Physical Review B 89, no. 23 (2014): 235319.
- [25] Qiao, Jingsi, Xianghua Kong, Zhi-Xin Hu, Feng Yang, and Wei Ji, *High-mobility transport anisotropy and linear dichroism in few-layer black phosphorus* Nature communications 5 (2014).
- [26] Low, Tony, Michael Engel, Mathias Steiner, and Phaedon Avouris, *Origin of photoresponse in black phosphorus phototransistors*, Physical Review B 90, no. 8 (2014): 081408.
- [27] Engel, Michael, Mathias Steiner, and Phaedon Avouris, *Black phosphorus photodetector for multispectral, high-resolution imaging*, Nano letters 14, no. 11 (2014): 6414-6417.
- [28] Buscema, Michele, Dirk J. Groenendijk, Sofya I. Blanter, Gary A. Steele, Herre SJ van der Zant, and Andres Castellanos-Gomez, *Fast and broadband photoresponse of few-layer black phosphorus field-effect transistors*, Nano letters 14, no. 6 (2014): 3347-3352.
- [29] Yuan, Hongtao, Xiaoge Liu, Farzaneh Afshinmanesh, Wei Li, Gang Xu, Jie Sun, Biao Lian et al, *Polarization-sensitive broadband photodetector using a black phosphorus vertical pn junction*, Nature nanotechnology (2015).
- [30] Youngblood, Nathan, Che Chen, Steven J. Koester, and Mo Li, *Waveguide-integrated black phosphorus photodetector with high responsivity and low dark current*, Nature Photonics (2015).
- [31] Castellanos-Gomez, Andres, Leonardo Vicarelli, Elsa Prada, Joshua O. Island, K. L. Narasimha-Acharya, Sofya I. Blanter, Dirk J. Groenendijk et al, *Isolation and characterization of few-layer black phosphorus*, 2D Materials 1, no. 2 (2014): 025001.
- [32] D.C. Chang, E.F. Kuester, *An analytic theory for narrow open microstrip*, Arch. Elektron. und Uebertragungstech. , 199 - 206

- [33] J. S. Bagby, C.-H. Lee, D. P. Nyquist, Y. Yuan, *Identification of propagation regimes on integrated microstrip lines*, IEEE Trans. Microw. Theory Tech., vol. 41, no. 11, pp. 1887-1894, Nov. 1993.
- [34] D. P. Nyquist, D. J. Infante, *Discrete higher-order leaky-wave modes and the continuous spectrum of stripline*, IEICE Trans., vol. E78-C, No. 10, pp. 1331-1338, Oct. 1995.
- [35] D. P. Nyquist, J. M. Grimm, D. J. Infante, and H. Braunsch, *Classification of the Proper Propagation-Mode Spectrum and Leaky-Wave Modes on Open Planar Waveguides*, Electromagnetics, 17, 2, 1997, pp. 105-130.
- [36] A. Ishimaru, *Electromagnetic Wave Propagation, Radiation, and Scattering*, Prentice Hall, 1991.
- [37] G.W. Hanson and A.B. Yakovlev, *An Analysis of Leaky-Wave Dispersion Phenomena in the Vicinity of Cutoff Using Complex Frequency Plane Singularities*, Radio Science, v. 33, pp. 803-820, July-Aug. (1998).
- [38] Lumerical Solutions, Inc. <http://www.lumerical.com/tcad-products/fdtd/>.
- [39] Olga V. Shapoval, Juan Sebastian Gomez-Diaz, Julien Perruisseau-Carrier, Juan R. Mosig, Alexander I. Nosich, *Integral Equation Analysis of Plane Wave Scattering by Coplanar Graphene-Strip Gratings in the THz Range*, IEEE Trans. Terahertz Sci. Technol. 3, 666 (2013).
- [40] C. S. R. Kaipa, A. B. Yakovlev, G.W. Hanson, Y. R. Padooru, F. Medina, and F. Mesa, *Enhanced transmission with a graphene-dielectric microstructure at low-terahertz frequencies*, Phys. Rev. B 85, 245407 (2012).
- [41] R. L. Haupt, D. H. Werner, *Genetic Algorithms in Electromagnetics*, Hoboken, NJ: Wiley, 2007.
- [42] Haupt, Randy L, *An introduction to genetic algorithms for electromagnetics*, IEEE Antennas and Propagation Magazine, Vol. 37, No. 2, April (1995).
- [43] F. Liang, A.B. Yakovlev, and G.W. Hanson, *Optimum Surface Plasmon Excitation and Propagation on Conductive Two-Dimensional Materials and Thin Films*, IEEE Trans. Antennas Propag., v. 63, pp. 1765-1774 (2015).
- [44] T. Low, R. Roldan, H. Wang, F. Xia, P. Avouris, *Plasmons and Screening in Monolayer and Multilayer Black Phosphorus*, Phys. Rev. Lett. 113, 106802 (2014).